Atomistic insight into the formation dynamics of charged point defects: A classical molecular dynamics study of F$^+$-centers in NaCl

Shuaishuai Yuan ◉,[1,*] Lev Kantorovich,[2] Alexander L. Shluger,[3] and Kirk H. Bevan ◉[1,4,†]

[1]*Division of Materials Engineering, Faculty of Engineering, McGill University, Montréal, Québec H3A 0C5, Canada*
[2]*Department of Physics, King's College London, Strand, London WC2R 2LS, United Kingdom*
[3]*Department of Physics and Astronomy, University College London, Gower Street, London WC1E 6BT, United Kingdom*
[4]*Centre for the Physics of Materials, Department of Physics, McGill University, Montréal, Québec H3A 2T8, Canada*

This paper provides an atomistic exploration of the lattice dissipation mechanisms accompanying the formation of charged point defects through a femtosecond resolved study of F$^+$-center creation in NaCl. Our findings, following from a classical molecular dynamics based investigation of this model system, point to general range of properties that should be present in similar systems. Immediately after the creation of such a charged defect center, its excess energy is imparted amongst the highest energy optical modes with no clear preference based on their degree of localization. This energy is then dissipated through equilibration amongst a bath of lower energy phonon modes. The temporal behavior primarily follows exponential decay trends at all the temperatures and energies explored, with a small degree of competition between phonon population and depopulation amongst lower energy bath modes. Moreover, the dissipation timescale is found to be approximately the same amongst all phonon energies. A temperature-dependent analysis shows the expected decrease in phonon lifetimes with increasing temperature. This is accompanied by similarly more rapid dissipation of thermal energy around the defect center at lower temperatures when the phonon mean free path is increased. An intuitive phenomenological model based on Langevin dynamics is also provided to interpret the atomistically derived phonon decay characteristics in the temporal domain. More broadly, these results are expected to aid the design and experimental investigation of strongly correlated materials where charged defect centers can play an important role in technological applications.

I. INTRODUCTION

Electronically driven lattice rearrangements often accompany the active operation of ionic and oxide materials within energy harvesting and conversion devices [1–8]. This includes phenomena such as electron/hole transfer, defect ionization, optical excitation, and even polaron formation [9–13]. When the loss, excitation, or transport of charge is associated with a single lattice site or thereabouts (e.g., via a defect center), the accompanying lattice dynamics often form an essential component in the manipulation of such energetic processes [6,14–17]. Thus, an atomistic understanding of the rearrangement dynamics associated with charge-state changes in point defects could significantly aid the design of energy materials [18,19]. Moreover, recent experimental advances in detecting lattice relaxation dynamics point to the need for furthering our atomic-scale understanding of such phenomena [15,20–27]. Following this vein of inquiry, we explore atomistically the manner in which a newly formed charged defect center relaxes its excess energy through dissipation within a surrounding lattice.

The lattice dynamics triggered by changes in the charge-state of a single lattice site typically involves the creation and annihilation of many phonons [15,20–26,28,29]. Over the past several decades, pioneering theoretical studies have explored the process of charged center relaxation via phonon dynamics in condensed-matter systems ranging from solids to liquids [30–34]. These analytical models have focused on the application of Fermi's golden rule to arrive at a phenomenological description of the phonon dissipation processes arising from the excitation or formation of charged defect centers [30–34]. Likewise, important model Hamiltonian developments have also provided crucial insights into the dynamical formation of small polaron-type charged defect centers via phonon interactions [35]. An important long-term goal in the field is to understand atomistically the mechanisms through which defect centers dynamically interact with their surrounding lattice [36,37]. By successively improving our atomistic models of the lattice rearrangements induced by charge defect centers, via refined interaction descriptions, further quantitative comparison with experiments should be achievable [15,20–26]. Such investigations would also serve to eventually reconcile both analytical and atomistic descriptions of charged defect centers and their lattice formation/excitation dynamics. Yet, atomistic studies focused on the dynamics of solid-state charged defect centers remain sparse [10,38–41]. This paper aims to further our atomic scale understanding of the lattice dynamics occurring during the formation of charged defect centers.

---

*shuaishuai.yuan@mail.mcgill.ca
†kirk.bevan@mcgill.ca
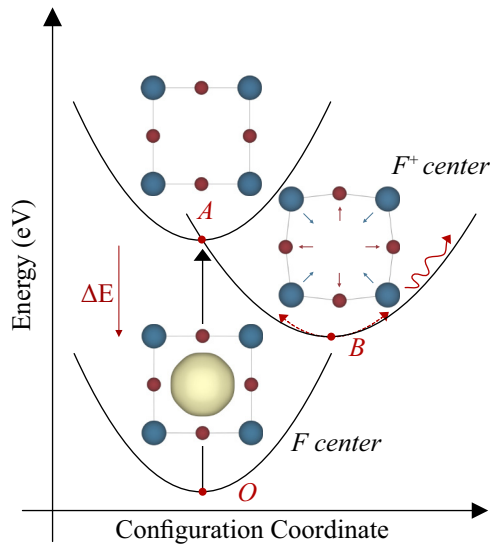
FIG. 1. Configuration coordinate diagram for charged color center formation in NaCl. The red balls represent Na atoms and the blue balls represent Cl atoms. The localized electron is shown in yellow. The image of the NaCl lattice is a 2D projection of the 3D lattice, which can better show the displacement of the atoms. The vertical transition from the initial (bottom) to the top potential energy surface with the minimum at the undistorted lattice (point A) corresponds to the ejection of the F center electron. After the electron is removed, the lattice distorts from the nonequilibrium configuration A to the equilibrium configuration B. Common to all charged defect centers, this transition from A to B is driven by lattice dynamics. The lattice coordinates and charge density of the localized electron (yellow ball) in this figure are directly obtained from DFT calculations that are detailed in Supplemental Material Sec. SA [47].

By adopting F^+-centers in NaCl as a model system (see Fig. 1) [20,28,42–46], we seek to address several unresolved questions pertaining to the formation dynamics accompanying charged defect centers. First, through what mechanisms does a defect center impart its excess energy within the phonon distribution and how does this energy relax/dissipate amongst the overall phonons via population/depopulation? Second, is there any preference or distinction between localized and delocalized phonon modes in the dissipative process? Third, what decay trends are exhibited in phonon dissipation dynamics? For example, do they decay exponentially in the temporal domain—with or without interplay between phonon population and depopulation over time, and what are the characteristic timescales? Fourth, how do population and depopulation characteristics vary as a function of phonon energy? Fifth, how do the dissipation trends in the local kinetic energy (local temperature) in the vicinity of such a defect differ from those in the phonon population? Lastly, how do these characteristics vary as a function of temperature? Crucially, these questions can only be fully addressed within the context of charged defect centers by also pursuing atomistic studies.

Across the computationally challenging length and timescales, we explore these points of inquiry within a classical molecular dynamics (MD) description of F^+-center formation via the following process (see Fig. 1): First, the F-center electron is ejected (the vertical O → A); this way

the excited electron is effectively removed from the system leaving behind an F^+-center in the nonequilibrium configuration A, which then relaxes to state B. It is this last process accompanied by the thermal relaxation that we study here. Our findings reveal that, though the overall dissipation process yields a complex substructure within the phonon relaxation dynamics, the general temporal decay trends can be captured by an intuitive description of a lattice equilibration. The highest energy phonon modes are shown to dominate in the release of energy to lower energy phonon modes acting as a bath—with the latter being weakly perturbed at the initial stage of defect formation. The overall phonon decay trends are found to be largely exponential in the temporal domain, with some competition between population and depopulation occurring in lower energy modes. Phonon lifetimes are shown to decrease with respect to temperature, while the local kinetic energy in the vicinity of the defect is shown to dissipate faster at lower temperatures. Collectively, these findings point to the important role that atomistic studies can provide in enhancing our understanding of charged defect center dynamics and associated lattice rearrangements driven by electronic processes.

The remainder of this paper is organized as follows. First, in Sec. II the computational details and analysis methods concerning our atomistic simulations are detailed. Then we present our results in Sec. III. We begin by examining lattice distortions between the initial and final configurations and their corresponding phonon mode decomposition in Sec. III A. This is followed by a detailed examination of dissipation dynamics including phonon decay dynamics and local temperature (kinetic energy) decay dynamics in Sec. III B. Then, in Sec. IV we present an intuitive framework based on Langevin dynamics for interpreting the general phonon decay and population/depopulation trends. A brief comparison between temperature dependence in the phonon-lifetime and a first-order analytical approach is also provided in Sec. IV. Finally, in Sec. V we present our conclusions and elaborate on points left for future investigation.

II. METHOD

A. Molecular dynamics approach

All results were obtained through classical MD simulations conducted within the LARGE-SCALE ATOMIC/MOLECULAR MASSIVELY PARALLEL SIMULATOR (LAMMPS) package [48]. Each MD run was prepared in four successive stages as illustrated in Fig. 2. We started at the pristine lattice geometry (no vacancy), choosing a large supercell employing periodic boundary conditions (details below). In stage I, the pristine lattice temperature was prepared near the target temperature following the approach of Estreicher *et al.* in Refs. [49,50]. This initial run period was held as a microcanonical (NVE) ensemble for 20 ps—the blue region in Fig. 2. Though very useful for initial thermalization, we found that this approach did not precisely achieve the desired target temperature due to lattice anharmonics. Thus, to ensure full phonon mode randomization at the target temperature, in stage II a canonical (NVT) ensemble with Langevin thermostat was applied for 50 ps at the target lattice temperature with a damping parameter magnitude of 0.1 ps—the red region in Fig. 2. In stage III,
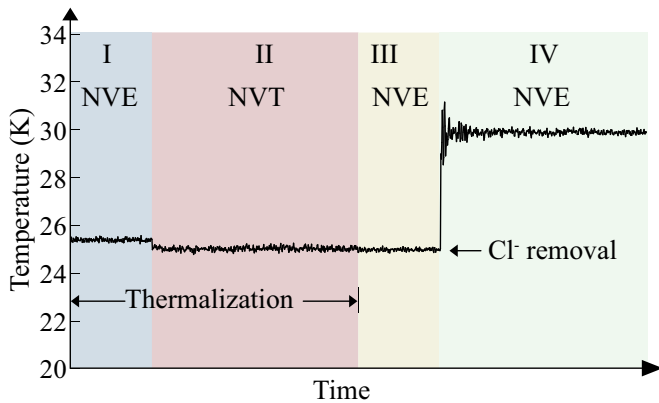
FIG. 2. Schematic of the MD run process at 25 K averaged over 40 samples. The process is conducted in stages I–IV. First, thermalization of the pristine lattice occurs in stages I and II. Then, partway into a fixed temperature NVE run a Cl^- atom is removed to mimic the formation of an F^+-center (stages III and IV, respectively). The temperature spike in stage IV and subsequent decay is due to the excess energy generated by the Cl^- atom removal and associated F^+-center relaxation dynamics. The same process is repeated at all temperatures, with the number of MD samples increasing with temperature.

the Langevin thermostat was turned off and the system was held as an NVE ensemble at constant lattice temperature for 20 ps—the yellow region in Fig. 2. In the final fourth stage, indicated in green in Fig. 2 and also held as an NVE ensemble, a Cl^- atom was removed to mimic the formation of an F^+-center due to electron ejection from the F-center (configuration A in Fig. 1). The dynamics of relaxation from configuration A to configuration B in Fig. 1 were then tracked both in real space and phonon space over a period of at least 20 ps within stage IV. Importantly, an NVE ensemble was employed to ensure that the relaxation process corresponds to a realistic situation in which the extra energy accumulated in the vacancy after excitation (modeled by the Cl^- removal) is able to dissipate into the rest of the crystal over the realistic timescales corresponding to anharmonic relaxations present in the system. We used this Cl^- ejection approach to approximately mimic the actual electron ejection process from the F-center, as bond lengths of the F-center defect are quite similar to that of the pristine lattice—this comparison is made in Supplemental Material Sec. SA [47]. Moreover, Cl^- ejection/removal was deemed more physically sound than attempting to capture the interactions of the partially delocalized electron in the F-center via a force-field potential. The duration of stages I–III could be optimized to be shorter. However, we have found that at least 20 ps is needed to track F^+-center relaxation dynamics in stage IV.

To capture atomic interactions within this classical MD framework, we utilized empirical Na^+ and Cl^- Buckingham potentials [51] of the form

$$U_{ij}(r) = \frac{Z_i Z_j e^2}{r} + A \exp\left[-\frac{r}{\rho}\right] - \frac{C}{r^6}. \quad (1)$$

Here r is the interatomic distance between atoms i and j, while Z_i and Z_j are their partial charges and e is the elementary charge. All force-field parameters are listed in Table SI

within the Supplemental Material [47] and were previously fitted to the experimentally determined elastic constants and crystal parameters of NaCl [51]. The resulting NaCl elastic properties calculated using this parametrization have been shown to match well with experiments [52]. Compared with experimental data and 0 K density functional theory (DFT) calculations, these potentials provide a quantitatively similar lattice constant and bulk modulus—see Table. SII in the Supplemental Material [47] and Refs. [51,53–59] therein. The phonon band structure obtained from these potentials can be found in Supplemental Material Sec. SI [47]. In terms of the overall phonon band structure trends, this approach excludes the splitting of the longitudinal and transverse optical modes at the Γ-point. However, the remaining phonon dispersion properties are quantitatively similar to those computed from first principles and measured experimentally [60–62]. Therefore, our approach based on using classical force fields must be appropriate for our purposes of capturing the main features of the thermalization process. The corresponding bulk phonon density of states (DOS) resulting from these potentials can be found in Supplemental Material Fig. S7 a(ii) [47].

All of the MD results presented in this main portion of the paper were obtained for a $6 \times 6 \times 6$ supercell consisting of 1727 atoms (or 1728 prior to removal of the Cl^- atom as shown in Fig. 2). Since relaxation dynamics were studied as a function of temperature T, rigorous statistical sampling had to be applied to ensure consistent trends. Details regarding the statistical sampling criteria employed are discussed in Sec. II B 2. Moreover, we found that a sufficiently large supercell size is needed to obtain physically consistent relaxation trends (i.e., from A to B as illustrated in Fig. 1). This was accomplished by achieving convergent relaxation lifetimes with respect to system size as discussed in Sec. II C. Importantly, the computational challenges arising from the timescale, system size, and degree of MD sampling needed to obtain physically meaningful insights were deemed to be too excessive for first-principles MD studies of the relaxation process at this time. This study is designed as an initial step toward more quantitative first-principles studies and is focused on obtaining qualitative atomistic insights into the relaxation dynamics associated with charged defect centers.

B. Decay tracking

In this analysis, we track how the decay process from configuration A to B occurs (as shown in Fig. 1) both in real space and phonon space. Both approaches are detailed below.

Our analysis is based on the idea of expanding atomic displacements $u_i(t)$ directly available during the course of MD simulations via normal modes of atomic harmonic vibrations corresponding to the final equilibrium configuration (B in Fig. 1). Higher-order terms in expanding the potential energy beyond the harmonic approximation describe anharmonic properties in the lattice and have proven quite useful for computing phonon lifetimes [63]. However, in this paper, only second-order force constants are utilized to analyze the dynamics within phonon populations. This consideration arises from the enormous expense the treatment of the third-order constants would entail: Our minimum system size consists of 1727 atoms in a $6 \times 6 \times 6$ supercell, as discussed above. This would then correspond to $\sim 1 \times 10^{11}$ third-order

force-constant matrix elements to compute—even an order of magnitude reduction via symmetry would still be substantial. If fourth-order force constants were accounted for, the number of terms would have extended into $\sim 1 \times 10^{14}$ [60]. Additional temperature-dependent considerations in the anharmonic terms would extend this computation burden much further [60,63]. For the above reasons, we restrict this atomistic study to tracking decay within the phonon eigenspace of configuration B shown in Fig. 1—considering only up to the second-order force constants at this time. Moreover, as our supercell is large (the minimum one is $6 \times 6 \times 6$ in size), we focus on tracking phonon decay at the supercell Γ-point only.

The harmonic normal modes are obtained as eigenvectors $\mathbf{e}_s = (e_{is})$ of the dynamical matrix $\mathbf{D}$:

$$\mathbf{D}\mathbf{e}_s = \omega_s^2 \mathbf{e}_s. \tag{2}$$

Here ω_s are vibrational frequencies shown in Supplemental Material Fig. S7 a(ii) [47]. The dynamical matrix $\mathbf{D}$ consists of matrix elements $D_{ij} = \Phi_{ij}/\sqrt{m_i m_j}$, with Φ_{ij} being the force constant matrix that is calculated directly from interatomic potentials detailed in the previous subsection and m_i is the atomic mass associated with the degree of freedom i. In this paper, the dynamical matrix is obtained using the finite difference method within the PHONOLAMMPS and PHONOPY packages [64,65].

Actual atomic displacements $u_i(t)$ and velocities $\dot{u}_i(t)$ produced during the course of MD simulations can then be projected onto the normal modes displacements $q_s(t)$ and velocities $\dot{q}_s(t)$ via

$$u_i(t) = \frac{1}{\sqrt{m_i}} \sum_s e_{is} q_s(t), \tag{3}$$

$$\dot{u}_i(t) = \frac{1}{\sqrt{m_i}} \sum_s e_{is} \dot{q}_s(t). \tag{4}$$

Here $q_s(t)$ serve as amplitudes in expanding the displacements via the normal modes. Exploiting the orthonormality of the vibrational eigenvectors, the amplitudes

$$q_s(t) = \sum_s \sqrt{m_i} e_{is} u_i(t) \tag{5}$$

can be extracted and therefore easily calculated during the MD run from the actual atomic displacements. Note that the amplitudes are time dependent. A similar expression exists for calculating the amplitudes $\dot{q}_s(t)$ in expanding the atomic velocities $\dot{u}_i(t)$. Analyzing these amplitudes in time is essential for understanding the energy redistribution within all modes during the course of the F^+-center relaxation (thermalization) when tracking the decay process from configuration A to B.

Each normal mode s carries the harmonic potential energy $U_s(t) = \frac{1}{2}\omega_s^2 q_s^2(t)$ and kinetic energy $K_s(t) = \frac{1}{2}\dot{q}_s^2(t)$, both being time dependent. The total energy of the given harmonic mode, $E_s = K_s + U_s$, will therefore change in time due to redistribution of the energy between the modes caused by anharmonicity in the system. The total energy of our system, $E_{\text{tot}} = K + U$, consists of the total kinetic energy of the vibrating ions, $K = \sum_s K_s$, and their potential energy,

$$U = \sum_s U_s + U_{\text{anh}}, \tag{6}$$

where U_{anh} is the corresponding anharmonic contribution that is always present in any realistic MD simulation.

1. Local temperature decay

Following conventional MD interpretations [66], kinetic energy can be related to the temperature T of the system via $\frac{N}{2}k_B T = K$, where N is the number of degrees of freedom within our system (i.e., three times the number of atoms) and k_B is Boltzmann's constant. Following this line of reasoning, one may take the kinetic energy for a subset of atoms and their corresponding velocities to define a local temperature T_l of the form

$$T_l(t) = \frac{1}{k_B N_l} \sum_{j=1}^{N_l} m_j \dot{u}_j^2(t), \tag{7}$$

where the corresponding summation is restricted to the N_l atomic degrees of freedom within some spherical region surrounding the F^+-center of interest. This T_l is then tracked in time (t) as the system decays from configuration A to B at various lattice temperatures—see Fig. 1.

2. Phonon population decay

In our NVE MD calculations of the decay process from configuration A to configuration B, the total energy E remains conserved. However, the specific energy in a given mode $E_s(t)$ changes dramatically in time t during equilibration and is tracked throughout the decay process. This is due to anharmonic processes that facilitate energy exchange between (harmonic) normal modes.

We have also found it quite useful to track the redistribution of energy amongst all phonon modes by defining an energetic phonon density of states of the form

$$\Upsilon(E, t) = \sum_{s=1}^{N} E_s(t) D_s(E),$$

$$E_{\text{tot}} = \int_0^\infty \Upsilon(E, t) dE, \tag{8}$$

where $D_s(E) = \delta(E - \hbar\omega_s)$ is the phonon density of states contribution by mode s. To provide a smooth curve when plotting $\Upsilon(E, t)$, we approximated each D_s as a single Gaussian [67] of the form

$$D_s(E) = \frac{1}{\sigma\sqrt{2\pi}} \exp\left[-\frac{1}{2}\left(\frac{E - \hbar\omega_s}{\sigma}\right)^2\right], \tag{9}$$

employing a broadening value of $\sigma = 0.5$ meV. When analyzing the quantity $\Upsilon(E, t)$, we found it necessary to sample it over many MD runs to eliminate the noise, especially at higher T; see below for details.

Particularly useful insights can be gleaned by tracking the system decay in $\Upsilon(E, t)$ from nonequilibrium configuration A to steady-state configuration B via

$$\tilde{\Upsilon}(E, t) = \Upsilon(E, t) - \bar{\Upsilon}(E),$$

$$\bar{\Upsilon}(E) = \frac{1}{t_r} \int_{t_{ss}}^{t_{\text{max}}} \Upsilon(E, t) dt, \tag{10}$$

where t_{ss} is the time at which the system has been determined to reach equilibrium in configuration B, t_{max} is chosen well into stage IV of the NVE run, and $t_r = t_{\text{max}} - t_{ss}$ corresponds

to the final part of stage IV in Fig. 2 in which the system is considered fully equilibrated in configuration B. Hence, $\bar{\Upsilon}(E)$ is the steady-state averaged form of $\Upsilon(E, t)$, and $\tilde{\Upsilon}(E, t)$ corresponds to the deviation from the equilibrium value decaying to zero over time during the thermalization from A to B. Through extensive benchmarking, we have found that physically consistent trends in $\tilde{\Upsilon}(E, t)$ are obtained with $t_{ss} = 10$ ps and $t_{max} = 20$ ps, though showing small variations (but the same physical trends) as t_{max} and t_{ss} are extended further. However, the values of t_{max} and t_{ss} are certain to change with different defect systems.

The steady-state distribution of $\bar{\Upsilon}(E)$ was also utilized to determine the degree of statistical MD sampling required at a given temperature as this quantity is highly sensitive to the number of MD runs performed for the sampling of $\tilde{\Upsilon}(E, t)$. Specifically, we utilized the root-mean-square (RMS) in $\tilde{\Upsilon}(E, t)$ defined over the domain of times when the system is considered equilibrated ($t_{ss} \leqslant t \leqslant t_{max}$):

$$\tilde{\Upsilon}_{RMS} = \sqrt{\frac{1}{t_r E_{max}} \int_0^{E_{max}} \int_{t_{ss}}^{t_{max}} [\tilde{\Upsilon}(E, t)]^2 \, dt \, dE}, \qquad (11)$$

where E_{max} was typically set at 3σ or so beyond the maximum value of $\hbar\omega_s$. Note that $\tilde{\Upsilon}_{RMS}$ is unitless, as $\Upsilon(E, t)$ defined by Eqs. (8). Typically, the value of $\tilde{\Upsilon}_{RMS}$ depends on the manner in which the mode density of states (D_s) is plotted. When setting $\sigma = 0.5$ meV in Eq. (9), consistent decay trends we determined result from $\tilde{\Upsilon}_{RMS} < 2.4$, which is considerably less than the maximum value of $\tilde{\Upsilon}$ arrived at with this value of σ. We mention these factors since the peak values of $\tilde{\Upsilon}$ (and necessary $\tilde{\Upsilon}_{RMS}$ noise tolerance) depend very much on the value of σ employed to plot the decay process. Moreover, minimizing noise is essential in Fig. 2. To meet these stringent noise criteria, we have found that as few as 40 MD samples can suffice at 25 K to properly sample $\tilde{\Upsilon}(E, t)$, while at least 6000 MD samples are needed at 300 K. Full details can be found in Supplemental Material Sec. SD [47]. These aspects will also be discussed further in Sec. III.

C. Decay fitting and system size

All decay lifetimes (τ), either for a phonon mode or the local temperature about the F^+-center, were determined through an exponential decay fit of the form

$$f(t) = C \exp(-t/\tau) + D, \qquad (12)$$

where C, D, and τ are fitting constants. For phonon mode lifetimes, we assigned $\tau = \tau_s$, whereas for the local temperature (T_l) lifetimes we assigned $\tau = \tau_l$. Fits were made for the decay from A to B starting from the point in stage IV when the Cl^- was removed (see Fig. 2).

Crucially, the convergence of lifetimes extracted via these exponential fits, via Eq. (12), was taken to be the primary criteria for determining the appropriate supercell size for this paper. There are two key issues associated with studying decay properties via a supercell approach. First, periodic boundary conditions can lead to the echoing of the relaxation distortion front at long timescales (i.e., > 1 ps). Second, small supercells typically dampen even the initial decay dynamics (i.e., <1 ps) improperly due to the magnitude of the energy be-

ing dissipated. For the potentials parameterized in this paper, the removal of a Cl^- atom to form an F^+-center is accompanied by the lattice relaxation which releases 2.19 eV of energy in a $6 \times 6 \times 6$ supercell. To determine the appropriate supercell size, it was successfully increased until the local temperature and phonon population decay trends were found to have converged. These convergence tests were performed at 50 K up to a cell size of $10 \times 10 \times 10$ (7999 atoms). We found it is important to perform such tests at low temperatures, where damping by the external lattice is less pronounced and the impact of the aforementioned computational issues can be clearly discerned. Detailed information regarding these convergent lifetime trends can be found in Supplemental Material Sec. SE [47].

III. RESULTS

A. Lattice distortion and phonon mode decomposition

Configuration A in Fig. 1 constitutes a nonequilibrium charged state, the energy of which is relaxed through the interaction with the lattice phonons. The dissipative transition from configuration A to B is accompanied locally around the center by an inward motion of Cl^- atoms (blue) and outward pushing of Na^+ (red) into new equilibrium positions, as shown in Fig. 1. Over longer length scales, the distortion interaction with the F^+-center follows this same directionality trend, as shown in the inset to Fig. 3(a). Specifically, the magnitude of the Cl^- and Na^+ displacements is progressively decreasing as one moves away from the defect [denoted as a shell index in Fig. 3(a)]. These trends are consistent with repulsive and attractive electrostatic interactions expected for a positively charged defect center in an ionic lattice.

The F^+-center distortion magnitude in Fig. 3(a) is projected to the phonon space of configuration B in Fig. 3(b). Here one can see the distortion magnitude is well distributed amongst all acoustic and optical phonon modes, with the exception of three higher energy optical modes captured in bold purple, blue, and black in Fig. 3(b) that are represented much stronger than others. The spatial character of these three prominent modes is provided in Fig. 4, where it can be seen that they are optical modes in nature and extend well beyond the defect center. Specifically, they belong to the highest energy optical modes (see Supplemental Material Sec. SI) [47]. The most localized of the three is situated at 9.1 THz [Figs. 4(a)–4(c,ii)]. Acoustic modes are only pronounced below ~5 THz (see Supplemental Material Sec. SI) [47]. The prominence of the high-energy optical modes in Fig. 3(b) is not entirely surprising, given that they all follow the same trend of opposing Cl^- and Na^+ displacements as the overall distortion and have the defect's symmetry. This can be seen by comparing Figs. 4(a)–4(c) with the inset in Fig. 3(a). The spatial character of some other modes introduced by the F^+-center and their localization measurement can be found in Supplemental Material Sec. SJ [47].

Next, let us turn to calculate the potential energy change imparted to each mode (δU_s) by the distortion via Eq. (6) as given in Fig. 3(c). Here we can see that the ω_s^2 contribution in Eq. (6) dramatically elevates the dissipative contribution of the higher energy optical modes. Those modes that are highlighted in bold in Fig. 3(b) take an especially large fraction
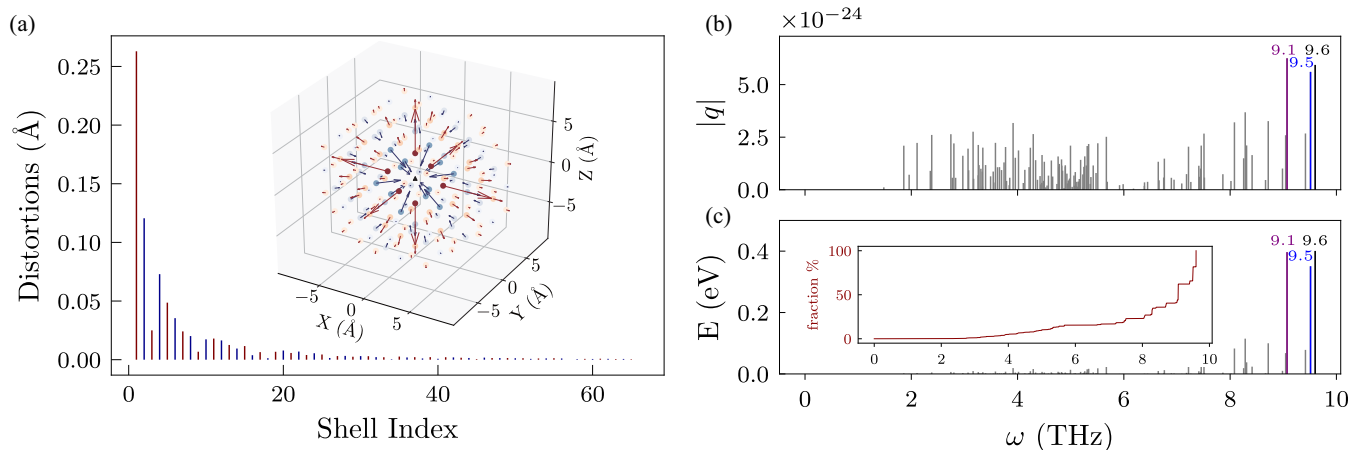
FIG. 3. (a) Atomic distortion magnitude around a relaxed F^+-center with respect to shell index, comprising the atomic displacement from A to B in Fig. 1. With increasing shell index, one moves progressively further away from the charged defect site. Atomic displacements within the first ten shells are shown as an inset, with vectors reflecting the magnitude of the displacement for a given atom. In both the atomistic view and distortion plot, Na ions are indicated in red and Cl ions are indicated in blue. (b) The distortion field magnitude is projected into the phonon space of configuration B in Fig. 1, prominent high frequency optical phonon modes at 9.1 THz, 9.5 THz, and 9.6 THz are highlighted in bold purple, blue, and black, respectively. (c) The potential energy change (δU_s) per phonon modes s (in configuration B) immediately after the removal of a Cl^- atom to form an F^+-center (also see Fig. 1). All results are obtained within a $6 \times 6 \times 6$ NaCl supercell consisting of 1727 atoms, with phonon modes calculated at the Γ point of the supercell. Inset to (c): The overall fraction of total potential energy contained by all modes below a given frequency.

of the total potential energy in Fig. 3(c) because their $|q_s|$ magnitude is twice that of comparable high-energy optical modes leading to a further factor of 4 increase in their potential energy compared to modes of similar frequencies [see Fig. 3(b)]. The cumulative distribution of energies amongst all modes can be found in the inset panel within Fig. 3(c) (red), where we see that the higher energy optical modes above ∼6 THz take approximately 80% of the total defect relaxation energy—also see Supplemental Material Fig. S7 [47]. Very similar trends to Fig. 3(c) can be found in larger supercells, as provided in Supplemental Material Sec. SF [47].

Though optical phonons represent the character of the distortion imposed by such a center (in the sense of opposite displacement of positively and negatively charged lattice sites, see Figs. 3 and 4), this is not the primary reason why they dominate during energy dissipation. At best, the high-energy optical modes only project twice the overall phonon magnitude $|q_s|$ compared to the vast litany of phonon modes to which the defect couples [see Fig. 3(b)]. Indeed, a great many of the phonon modes to which the distortion projects substantially via $|q_s|$ lie in the acoustic range below 5 THz as shown in Fig. 3(b) [see also Supplemental Material Fig. S7 a(ii)] [47,62]. Rather, higher energy modes dominate energy dissipation primarily because their corresponding potential energy contribution via Eq. (6) increases quadratically with ω_s^2 [see again Fig. 3(c)]. Moreover, their localization association with the defect center appears to be weakly correlated with the energy imparted (see Figs. 3 and 4). This can be seen by comparing the localization trends of the higher energy modes in Fig. 4 with their imparted energies in Fig. 3(c).

B. Dissipation dynamics

1. Phonon decay dynamics

The phonon dynamics associated with the formation of an F^+-center are presented in Fig. 5. Here the phonon population

change, at various temperatures from 25 K through to 300 K, is depicted as the system transitions from configuration A to B (see also Fig. 1). This phonon population is plotted in the form of the energetic phonon DOS perturbation ($\tilde{\Upsilon}$) from the steady state as discussed in the context of Eqs. (8)–(10). The steady state (in configuration B) is assumed to have been reached after 10 ps, while configuration A at $t=0$ is viewed as a perturbation from steady state. Across all temperatures in Fig. 5 a striking consistent trend can be seen. A great majority of the lattice distortion energy initially present in configuration A (also see Fig. 3) is depopulated/annihilated (red through green, $\tilde{\Upsilon} > 0$) through the population/creation (blue, $\tilde{\Upsilon} < 0$) of lower energy acoustic and optical phonon modes below ∼6 THz.

The distribution of lower energy phonons which are populated (blue in Fig. 5) qualitatively mirrors the bulk phonon DOS distribution at and below ∼ 6 THz in Supplemental Material Fig. S7 a(ii) [47]. Specifically, the most prominent phonon creation peak at all temperatures in Fig. 5 occurs at the same energy as the bulk DOS peak in Supplemental Material Fig. S7[47]. Indeed, a correlation between the phonon DOS and decay dynamics is expected from first-order models of phonon dissipation dynamics in defect centers [29–32,71]. Due to zone folding the Γ-point phonon DOS in a $6 \times 6 \times 6$ supercell is a fair approximation to the bulk phonon DOS— see Supplemental Material Sec. SG and Sec. SI [47].

A closer examination of the phonon dynamics toward steady-state (configuration B) at frequencies below 6 THz reveals a more complex interplay between creation and annihilation dynamics in Fig. 5. At $t=0$, within this THz range phonon creation ($\tilde{\Upsilon} < 0$) clearly dominates, as energy is rapidly dissipated from the high energy optical modes. Yet, at longer time scales in Fig. 5(b) (e.g., toward $t=2.5$ ps at 50 K), we see that minor phonon annihilation ($\tilde{\Upsilon} > 0$) processes also occur. This is not entirely unexpected since
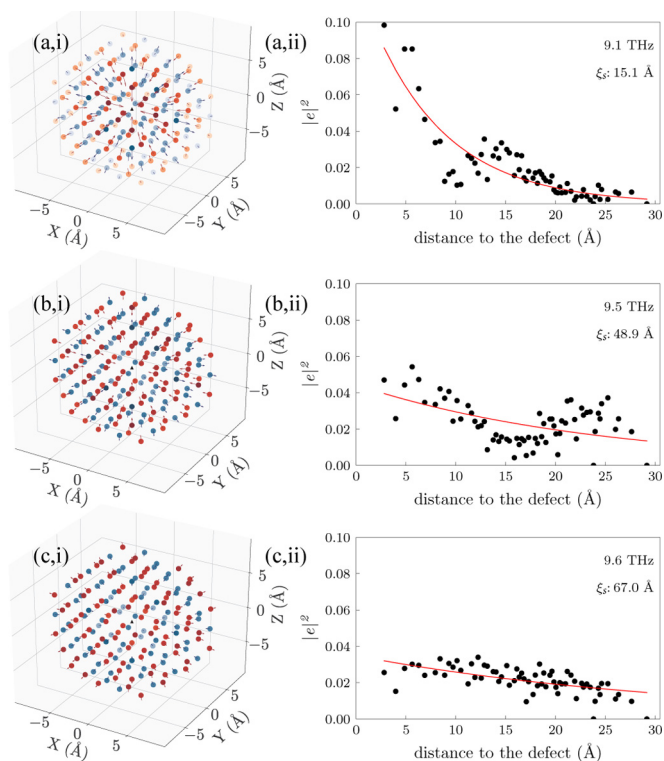
FIG. 4. (a)–(c,i) Configuration B eigenvector ($\boldsymbol{e}_s$) patterns of the most prominent three high-frequency phonon modes in Fig. 3(b) (for the distortion to configuration A from B). To enhance clarity, the displacement pattern of each mode is only projected around the first ten shells about the F^+-center. Na and Cl atoms are marked by red and blue, respectively, and darker colors indicate larger relative displacements within a given mode. The arrows illustrate the relative directions and magnitudes of phonon displacements. (a)–(c,ii) Spatial decay of the three high-frequency phonon modes. Here the Cl^- vacancy is set as origin. The black dots are $|\boldsymbol{e}_s(\mathbf{R}_n)|^2$ at each distance normalized by the number of atoms at distance $\mathbf{R}_n$. The red lines are fitted lines in the form $\propto \exp(-2|\mathbf{R}_n|/\xi_s)$, with the localization length ξ_s indicated in the upper right corner of each plot [68]. Details regarding other defect-induced modes and their localization characteristics are provided in Supplemental Material Sec. SJ [47] and Refs. [68–70] therein.

FIG. 5. F^+-center formation dynamics associated with the transition from configuration A to B in phonon space (see also Fig. 1). (a)–(h) Provide the energetic phonon DOS perturbation $\tilde{\Upsilon}(E, t)$, from the calculated steady-state population $\tilde{\Upsilon}(E)$ in configuration B, at various initial lattice temperatures from 25 K to 300 K. At 0 ps, the system is in configuration A just after removal of the Cl^- atom, while steady state in configuration B is assumed to have been reached at 10 ps. MD sampling was set to maintain $\tilde{\Upsilon}_{RMS} < 2.4$ at all temperatures. Phonon populations that are annihilated during the decay to steady state have a value of $\tilde{\Upsilon}(E, t) > 0$, while phonon populations that are enhanced during the dissipation process have values of $\tilde{\Upsilon}(E, t) < 0$. All results are for the Γ point in a $6 \times 6 \times 6$ supercell.

$\sim 20\%$ of the energy imparted at configuration A occurs below 6 THz [see Fig. 3(c)]. Meaning, these modes also have excess energy to dissipate, and creation-annihilation interchange, therefore, takes place within the bulk dynamics during equilibration toward configuration B (see Fig. 1). With the increasing temperature in Figs. 5(a)–5(e), the primary features associated with phonon dynamics below 6 THz display increasingly more rapid decay toward steady state (configuration B). However, the temperature-dependent variation in equilibration features below 6 THz becomes less pronounced at temperatures 200 K and above, as shown in Figs. 5(f)–5(h).

As mentioned above, the annihilation dynamics associated with higher energy optical modes shows prominently in red through green in Fig. 5. The most prominent annihilation peak at ~ 9.5 THz in Fig. 5 is due to the clustering overlap of several high-frequency modes that take a large proportion of the distortion energy, as shown earlier in Fig. 3(c). The

second prominent annihilation peak is at ~ 9.1 THz, and it is the mode with the highest degree of spatial localization among the three dominant optical phonon modes (see Fig. 4). Compared with other local modes shown in Sec. SJ [47], during the dissipation dynamics, the mode at 9.1 THz is the
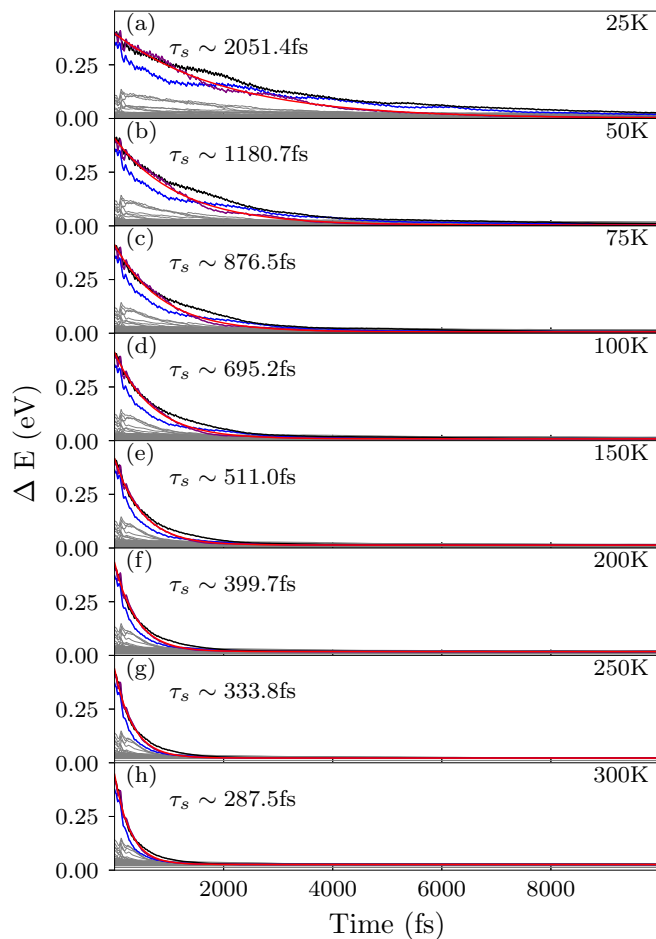
FIG. 6. (a)–(h) Phonon mode decomposed dissipation of the total energy during equilibration from A to B in Fig. 1 from 25 K to 300 K. The three most prominent phonon modes at 9.1 THz, 9.5 THz, and 9.6 THz are plotted in purple, blue, and black, respectively. All other modes are plotted in grey. An exponential fit of the form provided by Eq. (12) to the D mode at 9.1 THz, colored in red with $\tau = \tau_s$, results in the time constants (τ_s) provided in (a)–(h). The initial lattice temperature in configuration A is also provided in (a)–(h).

most dominant local mode associated with the defect, and thus we denote it as the D mode. When taken individually, the three dominant optical modes (see Fig. 4) each follows very similar temporal exponential decay of the form given by Eq. (12). In Fig. 6, the lifetime (τ_s) of the the D mode at 9.1 THz has been extracted by fitting Eq. (12). Such decay behavior, summarized by Eq. (12), is characteristic of Langevin dynamics as we shall discuss shortly in Sec. IV A. Hence, phenomenologically speaking, we can view each of the prominent high energy phonon modes coupled to the defect [see Fig. 3(c)] as collectively damped by the bath of lower energy modes that are created below 6 THz in Fig. 5 [3,35,72].

Exponential decay fits, via Eq. (12), to the D mode at 9.1 THz are provided in Fig. 6. These fits taken collectively as a function of temperature provide the phonon lifetimes in Fig. 7 (red squares). Very similar trends can be obtained for all the prominent optical modes above 6 THz in Figs. 3–6. From the temperature-dependent trends in Figs. 5 and 7, one can see that an anharmonic coupling
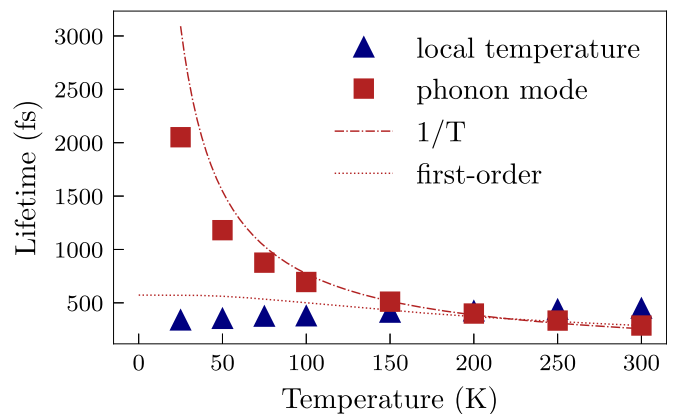
FIG. 7. Lifetimes as a function of the initial lattice temperature obtained for a $6 \times 6 \times 6$ supercell. Temperature-dependent phonon lifetime of the D mode at 9.1 THz (τ_s, red squares) and local lattice temperature lifetime (τ_l, blue triangles). A $1/T$ fit to the phonon lifetime is provided as a dot-dashed red line. Similarly, a first-order quantum rate fit is provided as a dotted red line.

between an annihilating/depopulating high-energy mode and the surrounding lattice has an increasing impact with rising temperature. This leads to increased dampening as the surrounding lattice temperature rises [73,74]. An increase in damping is manifest as a decrease in the phonon lifetime (τ_s) with respect to increasing temperature, as shown in Fig. 7 for the D mode [30–32,69,72]. Interestingly, the phonon lifetime decreases proportionally with respect to the inverse temperature in the manner of $1/T$ which is provided as a dot-dashed red line in Fig. 7 from 25 K through to 300 K—a trend discussed further in Sec. IV. Little change in the phonon lifetime occurs from 200 K through to 300 K, as can be seen in both Figs. 6 and 7. Most of the lifetime variation occurs from 25 K through to 150 K in Figs. 6 and 7. Moreover, since these results follow from classical MD calculations, excluding quantum-derived phonon transitions, any lifetime estimates in Fig. 7 as $T \to 0$ should be treated with caution [30–32,69–71,75]. This is a point we shall come back to in Sec. IV.

It is important to recognize that the phonon decay features in Figs. 5 through 7 should be taken as indicative of the dynamics that will present in the infinite bulk. The number of modes participating in the dissipation process increases with the system size examined (e.g., beyond $6 \times 6 \times 6$). Hence, in larger supercells, more high-energy optical modes above 6 THz will drive the annihilation dynamics presented in Figs. 5 and 6. Likewise, the creation dynamics below this frequency will span a broader range of modes in larger supercells. Nevertheless, the central trends presented remain as discussed in Sec. II C and presented in Supplemental Material Sec. SE [47].

2. Local temperature decay dynamics

Now, if we return to examining the spatial distribution of the three dominating optical modes in Fig. 4, it can be seen that even the D mode at 9.1 THz extends well beyond the defect center itself. Thus, the decay rate of a delocalized phonon mode is not necessarily indicative of energy dissipation in the vicinity of such a defect. For example, 78% of
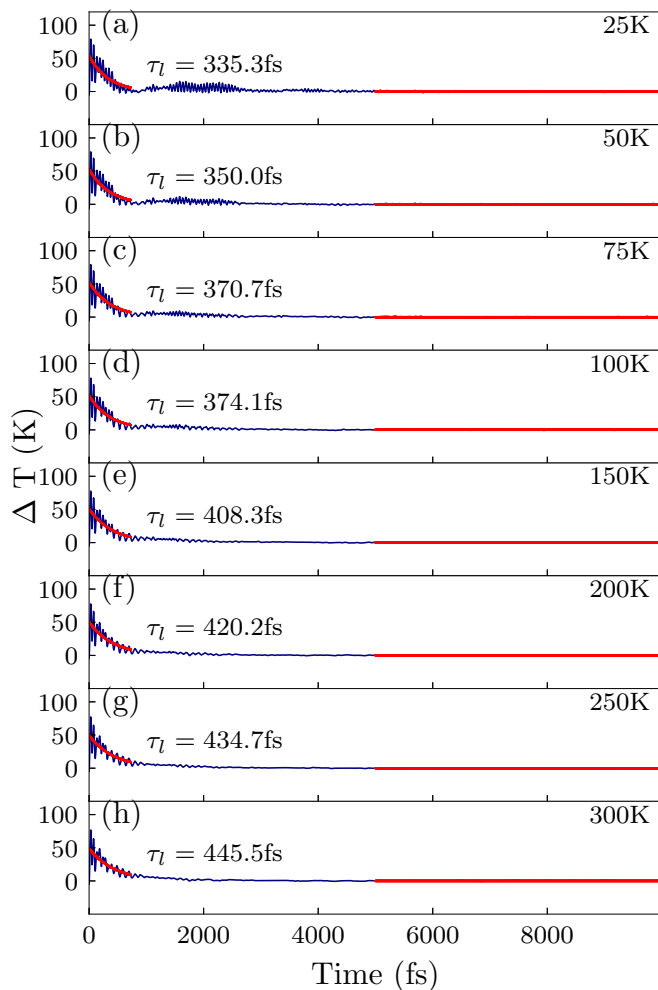
FIG. 8. (a)–(h) Local temperature dissipation within the first ten shells closest to the F^+-center during equilibration from A to B in Fig. 1. The selected region corresponds to 169 atoms amongst 1727 total in the $6 \times 6 \times 6$ supercell. Each local temperature (shown in blue) is fitted with an exponential decay (marked in red); the corresponding fit time constant is shown in each panel. Fitting takes the form of Eq. (12) with $\tau = \tau_l$. The data is only fitted prior to the emergence of interference due to periodic boundary conditions. The corresponding initial lattice temperature in configuration A is also provided in (a)–(h) at zero time. Larger supercells show very similar trends.

the F^+-center distortion is localized within just the first ten atomic shells around it (see Fig. 3(a) and also Supplemental Material Sec. SH [47] to this paper). Hence, a more informed description of how energy dissipation impacts upon the defect itself can be obtained by also extracting the local temperature (T_l) decay in the vicinity of the defect as summarized by Eq. (7) and provided in Fig. 8. Here we plot local temperature change within the first ten shells for a duration of 10 ps at various initial lattice temperatures ranging from 25 K to 300 K. Strikingly, Fig. 8 demonstrates that the local temperature lifetime (τ_l) is reduced at low temperatures and then rises only slightly at higher temperatures (see Fig. 7, blue triangles). This τ_l trend is precisely opposite to the phonon lifetime trends presented in Figs. 6 and 7, which are longest

at low temperatures and decrease with increasing temperature (see Fig. 7, blue triangles).

The temperature-dependent lifetime trends in T_l (Fig. 7) can be attributed to competing physical factors. First, more rapid transportation of the distortion energy away from the defect occurs at low temperatures when the phonon mean-free path is quite long. This leads to shorter local temperature lifetimes at lower temperatures rather than at higher temperatures. At lower temperatures, the imparted phonon energy can transport more rapidly away from the defect. Yet within the vicinity of the defect, a competition between increased phonon decay rate (see Fig. 5) and the decreased phonon mean-free path leads to a saturation trend in the T_l lifetime as higher external lattice temperatures are reached (Fig. 7, blue triangles) [73,76]. Stated more concisely, at higher lattice temperatures the energy dissipates more rapidly into the surrounding lattice (as evident by the decreased phonon lifetime at higher temperatures in Fig. 6) but also has greater difficultly in transporting away from the region surrounding the defect [73,76–78].

To obtain the local temperature lifetime (τ_l) estimates in Figs. 7 and 8, we conducted an exponential fit of the same form given in Eq. (12) with $\tau = \tau_l$. However, fitting (shown in red in Fig. 8) was only conducted up to the emergence of boundary propagation interference. In a $6 \times 6 \times 6$ supercell, this interference begins around 1 ps in Fig. 8(b) at 50 K, taking the form of rapid oscillations, and is progressively damped as the lattice temperature increases [see Figs. 8(a) through 8(h)]. Essentially, this interference arises from lattice waves echoing back into the defect region after propagating to the simulation cell boundaries. In smaller supercells, likely necessary to pursue first-principles calculations of such systems, open boundary conditions may be employed to overcome this difficulty [79–82]. As discussed in Sec. II C, through extensive benchmarking we have found that a sufficiently large supercell size is needed such that the decay process in Fig. 1 converges to a consistent damping lifetime. Larger supercell benchmarking of the trends in Fig. 8 can be found in Supplemental Material Sec. SE [47].

IV. DISCUSSION

The findings in Figs. 5–8 are connected through the common theme of phonon dynamics. At low temperatures, phonon-phonon scattering is reduced, leading to a longer phonon mean-free path. This results in longer phonon lifetimes at lower temperatures, thereby providing the trends in Figs. 5–7. Similarly, at lower temperatures a longer phonon mean-free path leads to the more rapid dissipation of thermal energy from around the defect center, likewise resulting in the local temperature trends found in Figs. 7 and 8. Thus, we would like to explore the energy dissipation trends arising from phonon dynamics further. To this end, we first present an analytical model that intuitively captures the phonon dissipation dynamics provided in Fig. 5. Subsequently, we explore the degree to which the temperature-dependent phonon trends in Fig. 7 can be captured by first-order phonon rate expressions. Higher-order theoretical avenues for future investigation are also discussed.

A. Analytically interpreting the phonon dissipation trends

During the transition from A to B in Fig. 1, the excess potential energy δU (which is present when the system resides in configuration A) is subsequently transformed into thermal energy through redistribution amongst all phonon modes. Hence, in the final steady-state equilibrium at B, each mode gains a mean thermal energy contribution of $\overline{\delta U_s}$ given by

$$\overline{\delta U_s} = \frac{1}{N}\sum_{s=1}^{N}\delta U_s, \qquad (13)$$

which in our $6 \times 6 \times 6$ supercell occurs over $N = 5181$ modes. The equilibrium redistribution in Eq. (13) can be compared to the excess nonequilibrium energy distribution for each mode δU_s (in configuration A) as presented in Fig. 3(c). Following the results of Figs. 5 and 6, we can further assume that all modes work in concert to approximately dissipate this excess energy in A as a first-order decay process of the form described by Eq. (12). Based on these assumptions, an analytical expression for the perturbation in the energetic phonon density of states given by Eq. (10) takes the form

$$\tilde{\Upsilon}(E,t) \approx \sum_{s=1}^{N}[\delta U_s[e^{-t/\tau_s}+\eta]\delta(E-\hbar\omega_s)-\overline{\delta U_s}]. \qquad (14)$$

This phenomenological model arises from treating the dissipation physics acting on each phonon mode (s) via Langevin dynamics of the form

$$\frac{d^2 q_s}{dt^2} = -\omega_s^2 q_s(t) - \frac{1}{\tau_s}\frac{dq_s}{dt} + \eta_s, \qquad (15)$$

$$\langle \eta_s(t) \rangle = 0, \qquad (16)$$

$$\langle \eta_s(t)\eta_s(t') \rangle = \frac{2k_B T_f}{\tau_s}\delta(t-t'), \qquad (17)$$

where η_s is the thermal noise driving each mode to the final equilibrated thermal energy of $k_B T_f/2 = \overline{\delta U_s} + k_B T/2$. Here T is the initial lattice temperature prior to the formation of the defect center.

To simplify the analysis, let us further assume that the decay time constant $\tau_s = \tau$ is approximately the same for all modes. This is based upon the similar decay trends demonstrated for annihilated/depopulated (red through green) and created/populated (blue) modes in Fig. 5. The term η is included in Eq. (14) to simulate the impact of random thermal noise, taking on an average value of zero—in a similar manner to η_s in Eq. (15). Plotting Eq. (14), employing the δU_s distribution in Fig. 3(c), we obtain the analytical $\tilde{\Upsilon}(E,t)$ result in Fig. 9(a). Impressively, this phenomenological model captures many of the physical trends present in the MD simulations. For comparison, the 50 K MD data set from Fig. 5(b) has been replotted next to it in Fig. 9(b)—with the time axis scaled by $\tau = 1180.7$ fs as determined from Fig. 6(b). It is important to note that the τ and δU_s values assigned in Eq. (14) all follow from the MD simulations and are not taken as adjustable parameters. Intriguingly, these decay trends are largely independent of temperature when normalized by the lifetime (τ) at a given temperature—see Fig. S11 [47]. This indicates that the same anharmonic physics is driving the temporal decay trends (amongst phonons) in the temperature ranges investigated.
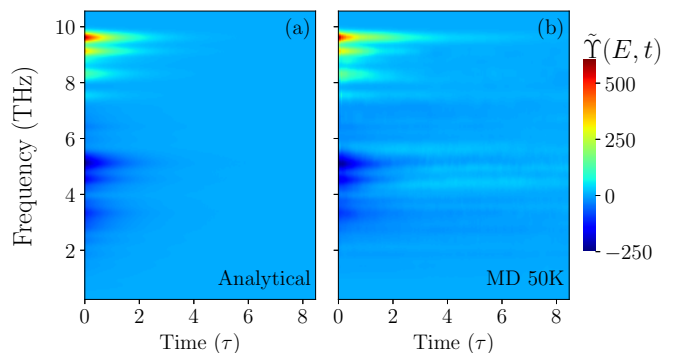
FIG. 9. (a) An analytical model of the energetic phonon DOS perturbation $\tilde{\Upsilon}(E,t)$ arising from defect relaxation compared to the molecular dynamics result at 50 K. (b) This MD result is the same as that in Fig. 5(b), normalized here with a time constant of $\tau_s = 1180.7$ fs for purposes of direct comparison.

In terms of energetics, Fig. 9 demonstrates that the distribution of annihilating/depopulating (red through green) and creating/populating (blue) modes are well captured by Eq. (14). Surprisingly, the temporal trends are also captured quite well by this first-order model. This is especially true for the highest energy modes around the D mode at 9.1 THz (red through green in Fig. 9) to which the decay time constant (τ) was fitted—also see Fig. 6. For the lower energy bath modes undergoing creation events (blue in Fig. 9), the general decay timescale found in the numerical and analytical plots agrees reasonably well. Though we caution that this agreement is likely an averaging/aggregation effect, as such individual phonon lifetimes (τ_s) are expected to vary about this mean (particularly for the bath of modes below 6 THz). Most prominently, the long timescale annihilation process below 6 THz, which are present beyond 3τ in the numerical result [light blue in Figs. 9(b) and S11 [47]], are excluded in the analytical model. This disagreement is to be expected as not all interactions acting on the lower energy modes are captured phenomenologically by Eq. (14), but might be with suitable modifications— a subject for future work.

B. Correspondence of phonon temperature dependence with first-order descriptions

The juxtaposition in Fig. 9 also lends further support toward viewing the lower energy modes below 6 THz as a bath into which excess energy from the highest energy optical modes is dissipated. Indeed, for this $6 \times 6 \times 6$ supercell, there are ~ 12 modes participating in creation dynamics below 6 THz for every mode likewise undergoing annihilation above 6 THz. Furthermore, given the dominance of creation processes below 6 THz, to first-order one may express the escape rate of energy into each such bath mode of energy $\hbar\omega_s < 6$ THz in the form

$$k_s = \frac{2\pi}{\hbar}|M|^2 D(\hbar\omega_s)[n(\hbar\omega_s)+1], \qquad (18)$$

which follows from Fermi's golden rule [29,32]. Here $|M|$ is the coupling for such a mode transition following from the anharmonic contributions summarized in Eq. (6), D is the phonon DOS, and $n(\hbar\omega_s) = [\exp(\hbar\omega_s/k_B T)-1]^{-1}$ is

the Bose-Einstien distribution for the phonon population [29,32]. Here we only consider the first-order creation of such bath states, since the results in Figs. 5 and 9 indicate that annihilation/depopulation events play a minor role below 6 THz. This threshold of 6 THz is entirely lattice dependent. Those modes with an initial energy (at $t = 0$) less than the final equilibrium lattice thermal energy $k_B T_f$ will be absorbing modes, as discussed in the context of Fig. 9 in Sec. IV A.

If we treat such a bath as an escape route for excess energy, then phenomenologically the total escape rate of energy into the bath can be approximated by

$$\frac{1}{\tau} = \sum_s k_s, \tag{19}$$

which is based upon the results in Fig. 9 where the system is well approximated as a first-order decay process [83]. Taking the DOS results computed for our $6 \times 6 \times 6$ supercell (see Supplemental Material Sec. SG [47]) and applying Eqs. (18) and (19), we arrive at the first-order lifetime (τ) result in Fig. 7 (dotted red). This is obtained by fitting the coupling term to $|M| = 3.5 \times 10^{-7}$ eV. This first-order description of the lifetime (τ) temperature dependence captures $1/T$ trends well above 200 K, but with less success at lower temperatures. At higher temperatures, we have $n(\hbar\omega_s) \propto T$, following from a Maclaurin series expansion, which explains the correspondence at 200 K and above. At lower temperatures, the $[n(\hbar\omega_s) + 1]$ factor in Eq. (18) correctly captures the quantum trends toward a finite lifetime as $T \to 0$, which is not present in either the $1/T$ fit or the MD results. It is the discrepancy between the MD results (red squares) and first-order rate expression (red dotted line) between 50 K and 150 K in Fig. 7 which clearly indicates the need for future investigations into a higher-order model [30–32]. To further reconcile analytical and atomistic lifetime calculations in this intermediate temperature regime, the first step would be to pursue lifetime calculations based on the third-order anharmonic terms as discussed in Sec. II and in Ref. [63]. Moreover, bulk atomistic studies have shown that the temperature dependence in the anharmonic coupling terms (in addition to the phonon populations) may impact temperature dependence of phonon lifetimes [60,63]. This temperature-dependent reconciliation between atomistic and analytical models is left for future work.

V. CONCLUSION

In this paper, we have examined the atomistic energy dissipation mechanisms associated with the formation of charged defect centers–with F^+-centers in NaCl adopted as a model system. Although the defect distortion was found to nearly equivalently perturb both high- and low-energy phonon modes, it was determined that the ω_s^2 proportional potential energy contribution leads to a large majority of the distortion energy being initially placed in the highest energy optical modes. Subsequently, through a temporal analysis of the energy redistribution amongst the phonon DOS, it was

determined that this excess energy in high-energy optical modes is dissipated through the creation of lower energy lattice modes acting as a bath. Moreover, by developing a first-order analytical model of phonon dissipation, the lifetime of this dissipation process was found to proceed on roughly the same timescale across all phonon energies and qualitatively follow Langevin dynamics. Moreover, the temporal decay characteristics were determined to be qualitatively very similar at all temperatures investigated—after normalizing by their decay time constant. Further analysis of the kinetic energy dissipation in the vicinity of the defect found that the locally generated heat dissipates more rapidly at lower lattice temperatures when the phonon mean-free path is longer. Correspondingly, at lattice higher temperatures the local defect kinetic energy (heat) dissipates more slowly due to increased phonon-phonon scattering. Similarly, the phonon lifetime was found to be largest at low temperatures and thereafter decrease proportionally to the inverse initial lattice temperature. This collection of general features is likely to be present in the relaxation of many charged defect systems. A first-order quantum rate model was also applied to further interpret the temperature dependence of the phonon lifetime. Good agreement was found beyond 200 K through the dominance of the phonon population distribution $n(\hbar\omega)$, yet less quantitative agreement was found with the first-order quantum rate model between 50 K and 150 K. It is likely that these shortcomings could be reconciled in future work on the calculation of phonon lifetimes through the atomistic investigation of higher-order anharmonic coupling terms and the inclusion of quantum effects [29–32,60,63].

It would also be quite interesting to extend this vein of investigation to understand the formation stages of small polarons, which are typically localized to approximately one lattice site as a charged defect center. In particular, it would be insightful to understand how analogous dissipation dynamics participate in the phonon dressing of small polaron centers [35,84]. However, this will likely require large-scale first-principles studies to adequately capture both the electron and lattice degrees of freedom. Similarly, large-scale first-principles studies of charged defects associated with lattice point defects (such as the F^+-center studied herein) will also likely prove useful in the endeavor toward quantitative predictions of such relaxation rates. These intriguing avenues of investigation are also left to future work.

[1] P. E. Trevisanutto, P. V. Sushko, K. M. Beck, A. G. Joly, W. P. Hess, and A. L. Shluger, Excitation, ionization, and desorption: How sub-band gap photons modify the structure of oxide nanoparticles, J. Phys. Chem. C **113**, 1274 (2009).

[2] N. Itoh and A. M. Stoneham, Materials modification by electronic excitation, Radiat. Eff. Defects Solids **155**, 277 (2001).

[3] A. Sugita, T. Saito, H. Kano, M. Yamashita, and T. Kobayashi, Wave Packet Dynamics in a Quasi-One-Dimensional Metal-Halogen Complex Studied by Ultrafast Time-Resolved Spectroscopy, Phys. Rev. Lett. **86**, 2158 (2001).

[4] B. J. Morgan and G. W. Watson, Polaronic trapping of electrons and holes by native defects in anatase TiO_2, Phys. Rev. B **80**, 233102 (2009).

[5] A. Alkauskas, Q. Yan, and C. G. Van de Walle, First-principles theory of nonradiative carrier capture via multiphonon emission, Phys. Rev. B **90**, 075202 (2014).

[6] H. Seo, Y. Ping, and G. Galli, Role of point defects in enhancing the conductivity of $BiVO_4$, Chem. Mater. **30**, 7793 (2018).

[7] S. Kim, S. N. Hood, and A. Walsh, Anharmonic lattice relaxation during nonradiative carrier capture, Phys. Rev. B **100**, 041202 (2019).

[8] X. Zhang, M. E. Turiansky, J.-X. Shen, and C. G. Van de Walle, Iodine interstitials as a cause of nonradiative recombination in hybrid perovskites, Phys. Rev. B **101**, 140101 (2020).

[9] A. Janotti, J. B. Varley, M. Choi, and C. G. Van de Walle, Vacancies and small polarons in $SrTiO_3$, Phys. Rev. B **90**, 085202 (2014).

[10] Z. Wang and K. H. Bevan, Exploring the impact of semicore level electronic relaxation on polaron dynamics: An adiabatic ab initio study of $FePO_4$, Phys. Rev. B **93**, 024303 (2016).

[11] K. H. Bevan, Electron transfer from the perspective of electron transmission: Biased non-adiabatic intermolecular reactions in the single-particle picture, J. Chem. Phys. **146**, 134106 (2017).

[12] S. Yuan, Z. Wang, M. L. F. Baron, and K. H. Bevan, Ab initio insight into the formation of small polarons: A study across four metal peroxides, Phys. Rev. B **100**, 205201 (2019).

[13] Y. Fan, Y. Lin, K. Wang, K. H. L. Zhang, and Y. Yang, Intrinsic polaronic photocarrier dynamics in hematite, Phys. Rev. B **103**, 085206 (2021).

[14] C. M. Yim, M. B. Watkins, M. J. Wolf, C. L. Pang, K. Hermansson, and G. Thornton, Engineering Polarons at a Metal Oxide Surface, Phys. Rev. Lett. **117**, 116402 (2016).

[15] C. Guo, X. Meng, H. Fu, Q. Wang, H. Wang, Y. Tian, J. Peng, R. Ma, Y. Weng, S. Meng, E. Wang, and Y. Jiang, Probing Nonequilibrium Dynamics of Photoexcited Polarons on a Metal-Oxide Surface with Atomic Precision, Phys. Rev. Lett. **124**, 206801 (2020).

[16] N. Daelman, M. Capdevila-Cortada, and N. López, Dynamic charge and oxidation state of Pt/CeO_2 single-atom catalysts, Nat. Mater. **18**, 1215 (2019).

[17] J. Yang, W. Li, D. Wang, and Y. Li, Single-atom materials: Small structures determine macroproperties, Small Struct. **2**, 2000051 (2021).

[18] D. Maarisetty and S. S. Baral, Defect engineering in photocatalysis: Formation, chemistry, optoelectronics, and interface studies, J. Mater. Chem. A **8**, 18560 (2020).

[19] J. S. Park, S. Kim, Z. Xie, and A. Walsh, Point defect engineering in thin-film solar cells, Nat. Rev. Mater. **3**, 194 (2018).

[20] T. Koyama and T. Suemoto, Dynamics of nuclear wave packets at the F center in alkali halides, Rep. Prog. Phys. **74**, 076502 (2011).

[21] Y. Qiu, K. B. Ucer, and R. T. Williams, Formation time of a small electron polaron in $LiNbO_3$: Measurements and interpretation, Phys. Status Solidi C **2**, 232 (2005).

[22] M. Ziwritsch, S. Müller, H. Hempel, T. Unold, F. F. Abdi, R. van de Krol, D. Friedrich, and R. Eichberger, Direct time-resolved observation of carrier trapping and polaron conductivity in $BiVO_4$, ACS Energy Lett. **1**, 888 (2016).

[23] L. M. Carneiro, S. K. Cushing, C. Liu, Y. Su, P. Yang, A. P. Alivisatos, and S. R. Leone, Excitation-wavelength-dependent small polaron trapping of photoexcited carriers in α-Fe_2O_3, Nat. Mater. **16**, 819 (2017).

[24] I. J. Porter, S. K. Cushing, L. M. Carneiro, A. Lee, J. C. Ondry, J. C. Dahl, H.-T. Chang, A. P. Alivisatos, and S. R. Leone, Photoexcited small polaron formation in goethite (α-FeOOH) nanorods probed by transient extreme ultraviolet spectroscopy, J. Phys. Chem. Lett. **9**, 4120 (2018).

[25] E. Pastor, J.-s. Park, L. Steier, S. Kim, M. Grätzel, J. R. Durrant, A. Walsh, and A. A. Bakulin, In situ observation of picosecond polaron self-localisation in α-Fe_2O_3 photoelectrochemical cells, Nat. Commun. **10**, 3962 (2019).

[26] J. S. Pelli Cresi, L. Di Mario, D. Catone, F. Martelli, A. Paladini, S. Turchini, S. D'Addato, P. Luches, and P. O'Keeffe, Ultrafast formation of small polarons and the optical gap in CeO_2, J. Phys. Chem. Lett. **11**, 5686 (2020).

[27] Y. Wang, M. Claassen, C. D. Pemmaraju, C. Jia, B. Moritz, and T. P. Devereaux, Theoretical understanding of photon spectroscopies in correlated materials in and out of equilibrium, Nat. Rev. Mater. **3**, 312 (2018).

[28] T. Tokizaki, T. Makimura, H. Akiyama, A. Nakamura, K. Tanimura, and N. Itoh, Femtosecond Cascade-Excitation Spectroscopy for Nonradiative Deexcitation and Lattice Relaxation of the Self-Trapped Exciton in NaCl, Phys. Rev. Lett. **67**, 2701 (1991).

[29] A. Tokmakoff, B. Sauter, and M. D. Fayer, Temperature-dependent vibrational relaxation in polyatomic liquids: Picosecond infrared pump–probe experiments, J. Chem. Phys. **100**, 9035 (1994).

[30] S. A. Egorov and J. L. Skinner, An improved theory of multiphonon relaxation in solids, J. Chem. Phys. **105**, 10153 (1996).

[31] S. A. Egorov and J. L. Skinner, On the theory of multiphonon relaxation rates in solids, J. Chem. Phys. **103**, 1533 (1995).

[32] V. M. Kenkre, A. Tokmakoff, and M. D. Fayer, Theory of vibrational relaxation of polyatomic molecules in liquids, J. Chem. Phys. **101**, 10618 (1994).

[33] A. Nitzan, S. Mukamel, and J. Jortner, Energy gap law for vibrational relaxation of a molecule in a dense medium, J. Chem. Phys. **63**, 200 (1975).

[34] J. Jortner, Direct vibrational relaxation of a molecule in a dense medium, Mol. Phys. **32**, 379 (1976).

[35] L. C. Ku and S. A. Trugman, Quantum dynamics of polaron formation, Phys. Rev. B **75**, 014307 (2007).

[36] W. H. Sio, C. Verdi, S. Poncé, and F. Giustino, Ab initio theory of polarons: Formalism and applications, Phys. Rev. B **99**, 235139 (2019).

[37] W. H. Sio, C. Verdi, S. Poncé, and F. Giustino, Polarons from First Principles, Without Supercells, Phys. Rev. Lett. **122**, 246403 (2019).

[38] G. Kolesov, B. A. Kolesov, and E. Kaxiras, Polaron-induced phonon localization and stiffening in rutile TiO_2, Phys. Rev. B **96**, 195165 (2017).

[39] K. Morita, T. Shibuya, and K. Yasuoka, Stability of excess electrons introduced by Ti Interstitial in Rutile TiO_2 (110) Surface, J. Phys. Chem. C **121**, 1602 (2017).

[40] M. Reticcioli, M. Setvin, M. Schmid, U. Diebold, and C. Franchini, Formation and dynamics of small polarons on the rutile TiO_2 (110) surface, Phys. Rev. B **98**, 045306 (2018).

[41] L. Zhang, Q. Zheng, Y. Xie, Z. Lan, O. V. Prezhdo, W. A. Saidi, and J. Zhao, Delocalized impurity phonon induced electron–hole recombination in doped semiconductors, Nano Lett. **18**, 1592 (2018).

[42] W. C. Holton and H. Blum, Paramagnetic resonance of *F* centers in alkali halides, Phys. Rev. **125**, 89 (1962).

[43] R. K. Swank and F. C. Brown, Lifetime of the excited *F* center, Phys. Rev. **130**, 34 (1963).

[44] R. Williams, R. Wilson, and Hanli Liu, Defects in alkali halides: Atomic force microscopy, cluster spectroscopy, and ultrafast time resolution, Nucl. Instrum. Methods Phys. Res., Sect. B **65**, IN8 (1992).

[45] W. Chen, C. Tegenkamp, H. Pfnür, and T. Bredow, Color centers in NaCl by hybrid functionals, Phys. Rev. B **82**, 104106 (2010).

[46] J. L. Gavartin, P. V. Sushko, and A. L. Shluger, Modeling charge self-trapping in wide-gap dielectrics: Localization problem in local density functionals, Phys. Rev. B **67**, 035108 (2003).

[47] See Supplemental Material at http://link.aps.org/supplemental/10.1103/PhysRevMaterials.6.015404 for other details on the formation dynamics of F^+ centers in NaCl.

[48] S. Plimpton, Fast parallel algorithms for short-range molecular dynamics, J. Comput. Phys. **117**, 1 (1995).

[49] S. K. Estreicher, D. West, J. Goss, S. Knack, and J. Weber, First-Principles Calculations of Pseudolocal Vibrational Modes: The Case of Cu and Cu Pairs in Si, Phys. Rev. Lett. **90**, 035504 (2003).

[50] S. K. Estreicher, T. M. Gibbons, B. Kang, and M. B. Bebek, Phonons and defects in semiconductors and nanostructures: Phonon trapping, phonon scattering, and heat flow at heterojunctions, J. Appl. Phys. **115**, 012012 (2014).

[51] C. R. A. Catlow, K. M. Diller, and M. J. Norgett, Interionic potentials for alkali halides, J. Phys. C: Solid State Phys. **10**, 1395 (1977).

[52] A. Nazmus Sakib and A. Adnan, On the size-dependent critical stress intensity factor of confined brittle nanofilms, Eng. Fract. Mech. **86**, 13 (2012).

[53] G. Kresse and J. Furthmüller, Efficiency of ab-initio total energy calculations for metals and semiconductors using a plane-wave basis set, Comput. Mater. Sci. **6**, 15 (1996).

[54] G. Kresse and J. Hafner, Ab initio molecular-dynamics simulation of the liquid-metal–amorphous-semiconductor transition in germanium, Phys. Rev. B **49**, 14251 (1994).

[55] G. Kresse and J. Furthmüller, Efficient iterative schemes for ab initio total-energy calculations using a plane-wave basis set, Phys. Rev. B **54**, 11169 (1996).

[56] G. Kresse and J. Hafner, Ab initio molecular dynamics for liquid metals, Phys. Rev. B **47**, 558 (1993).

[57] J. P. Perdew, K. Burke, and M. Ernzerhof, Generalized Gradient Approximation Made Simple, Phys. Rev. Lett. **77**, 3865 (1996).

[58] W. A. Bassett, T. Takahashi, H. Mao, and J. S. Weaver, Pressure-induced phase transformation in NaCl, J. Appl. Phys. **39**, 319 (1968).

[59] N. Kana, S. Khamlich, J. B. Kana Kana, and M. Maaza, Peculiar surface size-effects in NaCl Nano-crystals, Surf. Rev. Lett. **20**, 1350001 (2013).

[60] N. K. Ravichandran and D. Broido, Unified first-principles theory of thermal properties of insulators, Phys. Rev. B **98**, 085205 (2018).

[61] R. M. Pick, M. H. Cohen, and R. M. Martin, Microscopic theory of force constants in the adiabatic approximation, Phys. Rev. B **1**, 910 (1970).

[62] G. Raunio, L. Almqvist, and R. Stedman, Phonon dispersion relations in NaCl, Phys. Rev. **178**, 1496 (1969).

[63] O. Hellman and I. A. Abrikosov, Temperature-dependent effective third-order interatomic force constants from first principles, Phys. Rev. B **88**, 144301 (2013).

[64] A. Carreras, phonolammps git repository, https://github.com/abelcarreras/phonolammps.

[65] A. Togo and I. Tanaka, First principles phonon calculations in materials science, Scr. Mater. **108**, 1 (2015).

[66] D. Frenkel and B. Smit, *Understanding Molecular Simulation*, 2nd ed. (Academic Press, San Diego, 2002).

[67] J. M. Soler, E. Artacho, J. D. Gale, A. García, J. Junquera, P. Ordejón, and D. Sánchez-Portal, The SIESTA method for *ab initio* order-*N* materials simulation, J. Phys.: Condens. Matter **14**, 2745 (2002).

[68] P. B. Allen, J. L. Feldman, J. Fabian, and F. Wooten, Diffusons, locons and propagons: Character of atomie yibrations in amorphous Si, Philos. Mag. B **79**, 1715 (1999).

[69] D. West and S. K. Estreicher, First-Principles Calculations of Vibrational Lifetimes and Decay Channels: Hydrogen-Related Modes in Si, Phys. Rev. Lett. **96**, 115504 (2006).

[70] D. West and S. K. Estreicher, Isotope dependence of the vibrational lifetimes of light impurities in Si from first principles, Phys. Rev. B **75**, 075206 (2007).

[71] J. M. Ziman, *Principles of the Theory of Solids* (Cambridge University Press, Cambridge, UK, 1972).

[72] J. M. Wiesenfeld, L. F. Mollenauer, and E. P. Ippen, Ultrafast Configurational Relaxation of Optically Excited Color Centers, Phys. Rev. Lett. **47**, 1668 (1981).

[73] C. Kittel, *Introduction to Solid State Physics* (Wiley & Sons, New York, 1976).

[74] A. Glensk, B. Grabowski, T. Hickel, J. Neugebauer, J. Neuhaus, K. Hradil, W. Petry, and M. Leitner, Phonon Lifetimes Throughout the Brillouin Zone at Elevated Temperatures from Experiment and *Ab Initio*, Phys. Rev. Lett. **123**, 235501 (2019).

[75] T. M. Gibbons, M. B. Bebek, B. Kang, C. M. Stanley, and S. K. Estreicher, Phonon-phonon interactions: First principles theory, J. Appl. Phys. **118**, 085103 (2015).

[76] G. Chen, *Nanoscale Energy Transport and Conversion: A Parallel Treatment of Electrons, Molecules, Phonons, and Photons* (Oxford University Press, New York, 2005).

[77] T. H. Geballe and G. W. Hull, Isotopic and other types of thermal resistance in germanium, Phys. Rev. **110**, 773 (1958).

[78] G. Chen and C. L. Tien, Thermal conductivities of quantum well structures, J. Thermophys. Heat Transfer **7**, 311 (1993).

[79] L. Kantorovich, Generalized Langevin equation for solids. I. Rigorous derivation and main properties, Phys. Rev. B **78**, 094304 (2008).

[80] L. Kantorovich and N. Rompotis, Generalized Langevin equation for solids. II. Stochastic boundary conditions for nonequilibrium molecular dynamics simulations, Phys. Rev. B **78**, 094305 (2008).

[81] H. Ness, L. Stella, C. D. Lorenz, and L. Kantorovich, Applications of the generalized Langevin equation: Towards a realistic description of the baths, Phys. Rev. B **91**, 014301 (2015).

[82] D. Toton, C. D. Lorenz, N. Rompotis, N. Martsinovich, and L. Kantorovich, Temperature control in molecular dynamic simu-

lations of non-equilibrium processes, J. Phys.: Condens. Matter **22**, 074205 (2010).

[83] A. F. Voter, Introdution to the kinetic Monte Carlo method, in *Radiation Effects in Solids*, edited by K. E. Sickafus, E. A. Kotomin, and B. P. Uberuaga (Springer, Netherlands, 2007), pp. 1–23.

[84] A. S. Alexandrov and J. T. Devreese, *Advances in Polaron Physics*, Springer Series in Solid-State Sciences (Springer-Verlag, Berlin, 2010), Vol. 159.